Key Points:

- Interactions of traveling atmospheric disturbances (TADs) cause unexpected thermospheric neutral wind speeds in the American equatorial and low-latitude sectors
- The effects resulting from a disturbed electric field and TADs were able to produce anomalous electron density distribution at low latitudes
- The variations in the ionospheric observational measurements recorded around 4 UT in Brazil on 24 April 2023 were explained by the passages of TADs

Correspondence to:
J. R. Souza,
jonas.souza@inpe.br

Author Contributions:
Conceptualization: J. R. Souza, P. Dandenault, R. B. Kerr, I. S. Batista, Q. Wu
Data curation: J. R. Souza, A. M. Santos, J. Riccobono, S. Kapali
Formal analysis: J. R. Souza, P. Dandenault, A. M. Santos, J. Riccobono, R. B. Kerr, I. S. Batista
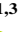**Funding acquisition:** J. R. Souza
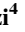
Impacts of Storm Electric Fields and Traveling Atmospheric Disturbances Over the Americas During 23–24 April 2023 Geomagnetic Storm: Experimental Analysis

J. R. Souza[1] , P. Dandenault[2] , A. M. Santos[1,3] , J. Riccobono[4] , M. A. Migliozzi[4] , S. Kapali[4], R. B. Kerr[4] , R. Mesquita[2] , I. S. Batista[1] , Q. Wu[5] , A. A. Pimenta[1] , J. Noto[6], J. Huba[7], L. Peres[8] , R. Silva[8], and C. Wrasse[1]

[1]National Institute for Space Research, São José dos Campos, Brazil, [2]Johns Hopkins University Applied Physics Laboratory, Laurel, MD, USA, [3]State Key Laboratory of Space Weather, NSSC/CAS, Beijing, China, [4]Computational Physics Inc., Lowell, MA, USA, [5]High Altitude Observatory, National Center for Atmospheric Research, Boulder, CO, USA, [6]Orion Space Solutions, Louisville, CO, USA, [7]Syntek Technologies, Fairfax, VA, USA, [8]Federal University of Western Pará, Santarém, Brazil

Abstract The paper presents the effects of the storm-time prompt penetration electric fields (PPEF) and traveling atmospheric disturbances (TADs) on the total electron content (TEC), foF2 and hmF2 in the American sector (north and south) during the geomagnetic storm on 23–24 April 2023. The data show a poleward shift of the Equatorial Ionization Anomaly (EIA) crests to 18°N and 20°S in the evening of 23 April (attributed to eastward PPEF) and the EIA crests remaining almost in the same latitudes after the PPEF reversed westward. The thermospheric neutral wind velocity, foF2, hmF2, and TEC variations show that TADs from the northern and southern high latitudes propagating equatorward and crossing the equator after midnight on 23 April. The meridional keograms of ΔTEC show the TAD structures in the north/south propagated with phase velocity 470/485 m/s, wave length 4,095/4,016 km and period 2.42/2.30 hr, respectively. The interactions of the TADs also appear to modify the wind velocities in low latitudes. The eastward PPEF and equatorward TADs also favored the development of a clear/not so clear F3 layer in northern/southern regions of the equator.

Plain Language Summary The thermosphere-ionosphere-magnetosphere system is largely affected during events of geomagnetic storms. Its dynamics, mainly in the ionized environment, may impact modern lives by degradations in the satellite signals affecting, for example, all applications involving Global Navigation Satellite System. The thermosphere and ionosphere responses to the large geomagnetic storm of 23–24 April 2023 are analyzed here and the main discoveries are the unexpected spatial plasma density distribution over Boa Vista (MLat ≈ 8°N) due to resulting effects of a disturbed eastward electric field and traveling atmospheric disturbance (TAD). The interactions/interferences of TADs were able to explain the unexpected moment of the peak in thermospheric neutral wind speed measurements over the equatorial station, as well as all variations in ionospheric parameters (foF2, hmF2, and total electron content) recorded in pairs by seven Digisondes and GNSS receivers spread across Brazil.

1. Introduction

A complete understanding of ionospheric dynamics during geomagnetically quiet conditions involves the competing effects of the dynamics of the neutral atmosphere and its own electric fields. Important players are thermospheric neutral winds and the electric fields of ionospheric dynamos (Kelley, 2009). The complexity of the competition increases, due to the increase in the number of players, for periods of geomagnetic disturbances and this has been studied for several decades, as pointed out by Fejer et al. (2024). The superposition of Traveling Atmospheric Disturbances (TADs), Disturbance Dynamo (DD), and prompt penetration electric fields (PPEFs) by undershielding or overshielding events over those of quiet time conditions frequently occurs during large geomagnetic storms. Recently, Fejer et al. (2024) published historical reports of the ionospheric electric field impacts from geomagnetic disturbances. In addition, they also discussed, in a clear and innovative way, the anomalous variations of the equatorial electric field during the 23 and 24 April 2023. In this work, a complementary investigation was carried out focusing on the response of the mid-lower-equatorial ionosphere to the same geomagnetic storm.

Investigation: J. R. Souza, P. Dandenault, A. M. Santos, J. Riccobono, M. A. Migliozzi, S. Kapali, R. B. Kerr, R. Mesquita, I. S. Batista, Q. Wu, A. A. Pimenta, J. Noto, J. Huba, L. Peres, R. Silva, C. Wrasse
Methodology: J. R. Souza, P. Dandenault, A. M. Santos, J. Riccobono, M. A. Migliozzi, S. Kapali, R. B. Kerr, R. Mesquita, I. S. Batista, Q. Wu, A. A. Pimenta, L. Peres, R. Silva
Project administration: J. R. Souza
Writing – original draft: J. R. Souza, P. Dandenault, A. M. Santos, J. Riccobono, M. A. Migliozzi, R. B. Kerr, I. S. Batista
Writing – review & editing: J. R. Souza, P. Dandenault, J. Riccobono, R. B. Kerr, R. Mesquita, I. S. Batista

It is well-known that the PPEFs are directed eastward (westward) on the dayside (nightside) for undershielding events that are in phase with those of the quiet-time ionospheric dynamo. The corresponding characteristics for overshielding and DD events are exactly the reverse of this, that is, to the west (east) on the dayside (nightside).

TADs and Traveling Ionospheric Disturbances (TIDs) are strongly related to each other, except for evidence of a no strong correlation in amplitudes (England et al., 2021). These cited authors separated the ionospheric measurements for analyzing TIDs and the thermospheric ones for TADs. We could consider such a classification, but that is outside our scope. One of the main scopes of our work is to prove that anomalous variations of thermospheric neutral winds are caused by TADs, their interactions/interferences and their simultaneous impacts on the ionosphere. Thus, although for mobile structures observed in ionospheric parameters are generally attributed to TIDs, here we will refer to TADs rather than TIDs. Several published scientific works have pointed out the characteristics of TAD/TID in which wave parameter values cover a wide range of variation. TADs have an oval auroral origin and propagate in the poleward and equatorial directions (Gardner & Schunk, 2010); reach maximum disturbances before or at the end of the main phase of the storm and can reach the equator in 1.5 hr (Balan et al., 2011); can cause wind waves with a preference for the night sector (Fuller-Rowell et al., 1994); the phase speed can be 291–1,070 m/s (Figueiredo et al., 2017); wavelength of 2,500 to 3,000 km (Gardner & Schunk, 2010); periods between 30 min and 3 hr (Hocke & Schlegel, 1996).

Simulations developed by Gardner and Schunk (2010) showed that TADs, with an oval auroral origin, can suffer interference in mid-latitudes after crossing the equator with unchanged speed. Guo et al. (2014) noted interference from TADs close to the equator and a near-perfect constructive case ($w1 + w2 = w1$) was identified. Pradipta et al. (2016) also reveal clear constructive wave interferences around the magnetic equator by a large-scale TID. The sum of the amplitudes of the two waves was not enough to explain the final result. They attributed it to an increase in the plasma density of the upper ionosphere due to the fountain effect. In our work, for a large and anomalous geomagnetic storm, wave interference was observed from low latitudes (MLat $\approx$ 20°S) to close to the magnetic equator during the period of absence of the fountain effect. Furthermore, all wave parameters were changed after interferences/interactions.

In fact, our main challenge here is to explain the thermospheric-ionospheric variations of the equatorial-low-mid latitudes involving the sectors of North, Central, and South America. The period of the investigation is 23–24 April 2023, during a geomagnetic storm characterized by large superMag ring current index (SMR is similar to SymH) and successive inversions of the interplanetary magnetic field. The ionospheric effects due to the subsequent immediate penetration of electric fields (undershielding followed by overshielding), and due to the strong variations in winds observed between the night of 23 April (F10.7 = 136.7 sfu) and the dawn on 24 April (F10.7 = 135.5 sfu), can be seen in Figure 1. This figure has two columns, one with information from 23 April and the other from 24 April. It is shown (from top to bottom) the following data: SMR index and solar wind dynamic pressure (first row); solar wind speed and interplanetary magnetic field (second row); vertical $\mathbf{E} \times \mathbf{B}$ plasma drift (third row); the thermospheric neutral winds for Arecibo, Santarém, and Cachoeira Paulista (CP) (rows 4, 5, and 6 respectively). It is interesting to highlight here the selected times of interest to us that are close to the two B_z inversions ~17:30 and ~21:00 UT, and the large neutral wind speed toward the equator around 4 UT. Two dashed pink bars mark the times of B_z inversion and the solid bar marks the time of maximum equatorward wind speeds. The solid black curves in panels 3–6 of Figure 1 were calculated by models and the values are representative of geomagnetically quiet conditions. The vertical $\mathbf{E} \times \mathbf{B}$ drifts were obtained from the empirical drift model developed by Scherliess and Fejer (1999) and the effective neutral wind from the Horizontal Wind Model (Drob et al., 2015). The effective wind (U_{eff}) is the result of the meridional (U_θ, *positive northward*) and zonal ($U_\varnothing$, *positive eastward*) components of the wind projected along the magnetic field, as given by

$$U_{\text{eff}} = (U_\theta \cos D + U_\varnothing \sin D) \cos I,$$

where D and I are magnetic declination (*positive eastward*) and dip angle, respectively.

2. Experimental Data, Their Organizations, and Keograms

The instruments whose measurements were used in our investigation are: one JULIA Medium Power Incoherent Scatter Radar (MP ISR), three Fabry-Pérot Interferometers (FPIs), seven Digisondes and 866 GNSS receivers. The GNSS receivers are from four different networks: CORS/USA, RBMC/Brazil, INCT/Brazil, and RAMSAC/
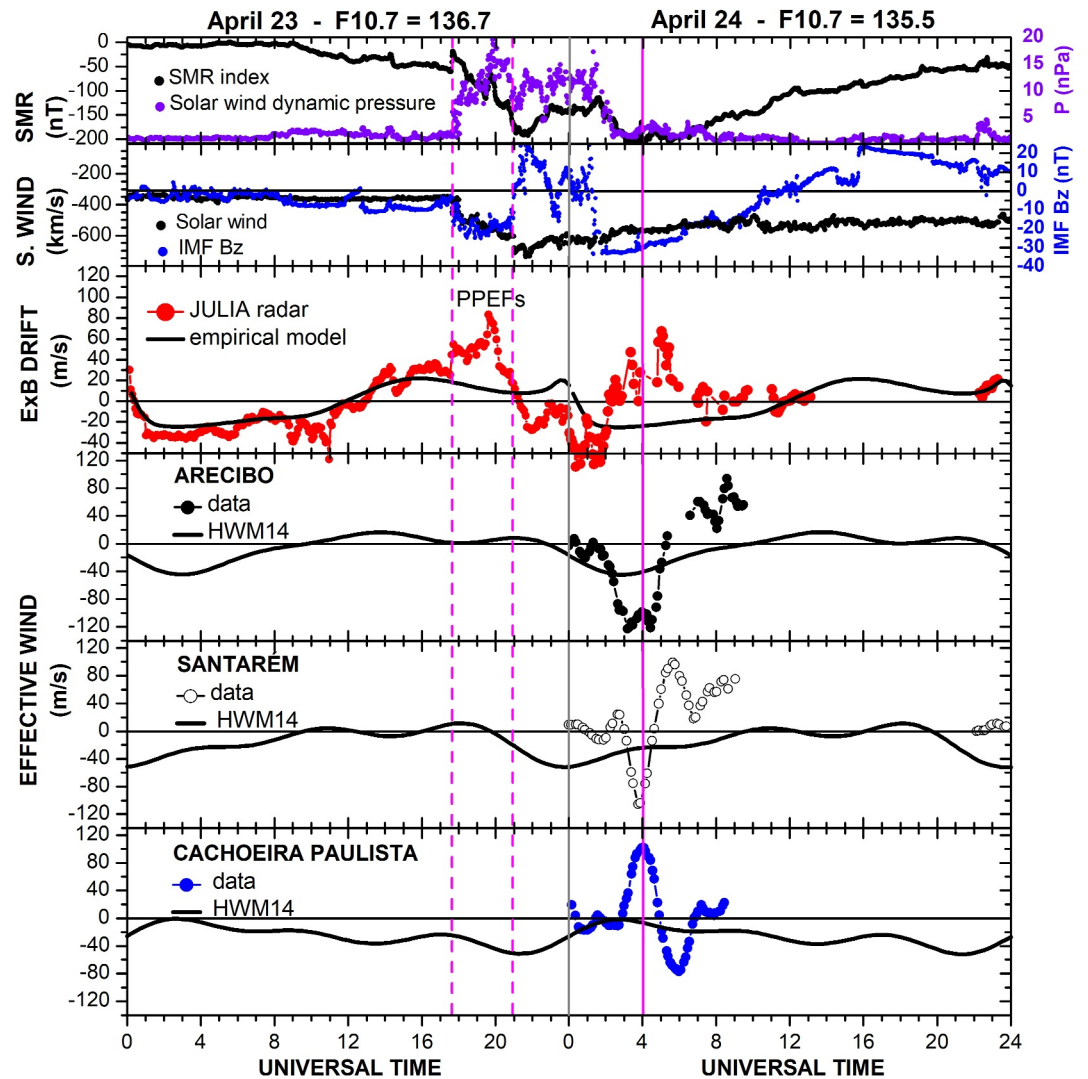
Figure 1. Diurnal variations of geomagnetic activity indices SMR, solar wind dynamic pressure (first row), solar wind velocity and interplanetary magnetic field—B_z component (second row), vertical $\mathbf{E} \times \mathbf{B}$ drifts (third row). Rows 4–6 are the thermospheric neutral wind speeds for Arecibo, Santarém, and Cachoeira Paulista, respectively. Data are for 23–24 April 2023.

Argentina. Figure 2 shows the location of each instrument. The left panel shows where the first instrument set is located, composed of FPIs, Digisondes, and the JULIA radar (The acronym JULIA stands for Jicamarca Unattended Long-term Investigations of the Ionosphere and Atmosphere, Hysell and Burcham (1998)). On the right side are the locations of the GNSS receivers, the second instrument set. The respective instruments have performed measurements of wind speed, $\mathbf{E} \times \mathbf{B}$ equatorial drift, F region peak parameters (foF2 and hmF2) and total electron content (TEC). The pink curves show the location of the magnetic equator, as calculated by the IGRF13 model (Alken et al., 2021) and the cyan-colored vertical bars are the geographic meridian selected to apply the keogram technique.

The numerical values of the locations, both in geographic and magnetic coordinates, for the first set of instruments are listed in Table 1. The magnetic coordinates were obtained from the website https://geomag.bgs.ac.uk. Instruments from the first set, their locations and data analyzes were separated into two groups (1 and 2) according to the response of hmF2 to the disturbance of meridional wind speeds after midnight on 23 April. At 04:00 UT hmF2 for Boa Vista (BV), Belém (BL), São Luís (SL), and Fortaleza (FZ) behave as if the winds were moving southward (Group 1, see Figure 3) while for Campo Grande (CG), CP and Santa Maria (SM) the winds were
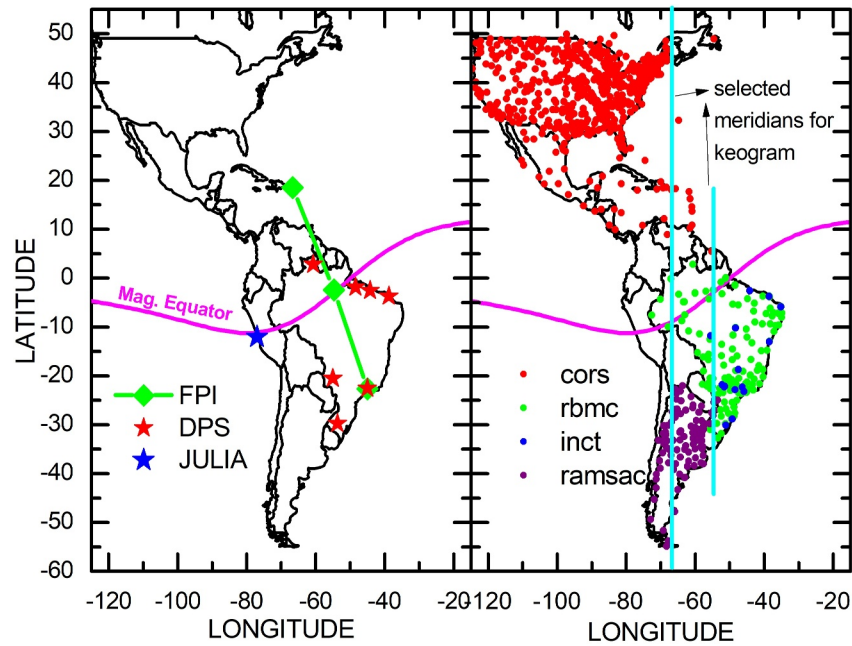
Figure 2. Maps with the positions of the Fabry-Pérot Interferometers, the JULIA radar and the Digisondes (DPSs) (on the left). Positions of the GNSS receivers of the CORS/USA, RBMC/Brazil, INCT/Brazil, and RAMSAC/Argentine networks are shown on right side. The vertical cyan bars indicate the selected meridians for applying the keogram technique.

moving northward (Group 2, see Figure 4). Since the winds over Arecibo (AR) and Santarém (ST) were flowing southward and Jicamarca (JI) is in the equatorial sector, they belong to Group 1.

The TEC data were interpolated using the method developed by Oliveira et al. (2020), which uses a spatial expansion with a median calculated to $1 \times 1°$ area during every 5 min and linear interpolations to fill data gaps. In this work only vertical TEC (vTEC) was used, therefore, when mentioned here, "TEC" indicates "vTEC." The keogram technique was used to investigate the presence of any propagating structure. The meridional keograms of ΔTEC were constructed by

$$\Delta\text{TEC} = \overline{\text{TEC}}_{3h20} - \overline{\text{TEC}}_{1h00},$$

where $\overline{\text{TEC}}_{3h20}$ and $\overline{\text{TEC}}_{1h00}$ are the respective running averages for time bins of 3 hr and 20 min and 1 hr.

3. Results and Discussions

The results are separated into Group 1 and Group 2, as mentioned previously. The focus here is to analyze the physical causes of anomalous, transient variations in thermospheric winds, ionospheric peak parameters (foF2 and hmF2) and TEC during the highest disturbance levels of a storm (as indicated by SMR, solar wind speed/dynamic pressure in Figure 1). A time window was selected starting at 16 UT on 23 April and ending at 8 UT of the following day, 24 April. This analysis is based on relative thermospheric-ionospheric changes compared to what happened in the same UT time interval during the day before the storm (22–23 April).

3.1. Ionospheric Effects of Undershielding and Overshielding Events and Disturbed Neutral Winds

Figures 3 and 4 show hmF2 for groups 1 and 2, respectively. The storm's electric field events occurred on 23 April, as shown in the left panels. Full

Table 1
Geographic and Magnetic Coordinates for Fabry-Pérot Interferometers, JULIA Radar and Digisondes (DPSs)

Station	Instrument	GLon (°)	Glat (°)	MLon (°)	MLat (°)
GROUP 1					
AR	FPI	293.3	+18.5	11.1	+25.3
BV	DPS	299.3	+02.8	13.9	+08.1
ST	FPI	305.5	−02.7	18.1	00.0
JI	JULIA	283.2	−12.0	356.0	−01.0
BL	DPS	311.6	−01.4	24.0	−02.2
SL	DPS	315.0	−02.5	27.4	−05.5
FZ	DPS	321.2	−03.7	32.0	−09.3
GROUP 2					
CG	DPS	305.3	−20.5	13.3	−14.9
CP	DPS/FPI	315.0	−22.7	21.1	−21.1
SM	DPS	306.2	−29.7	12.9	−22.9
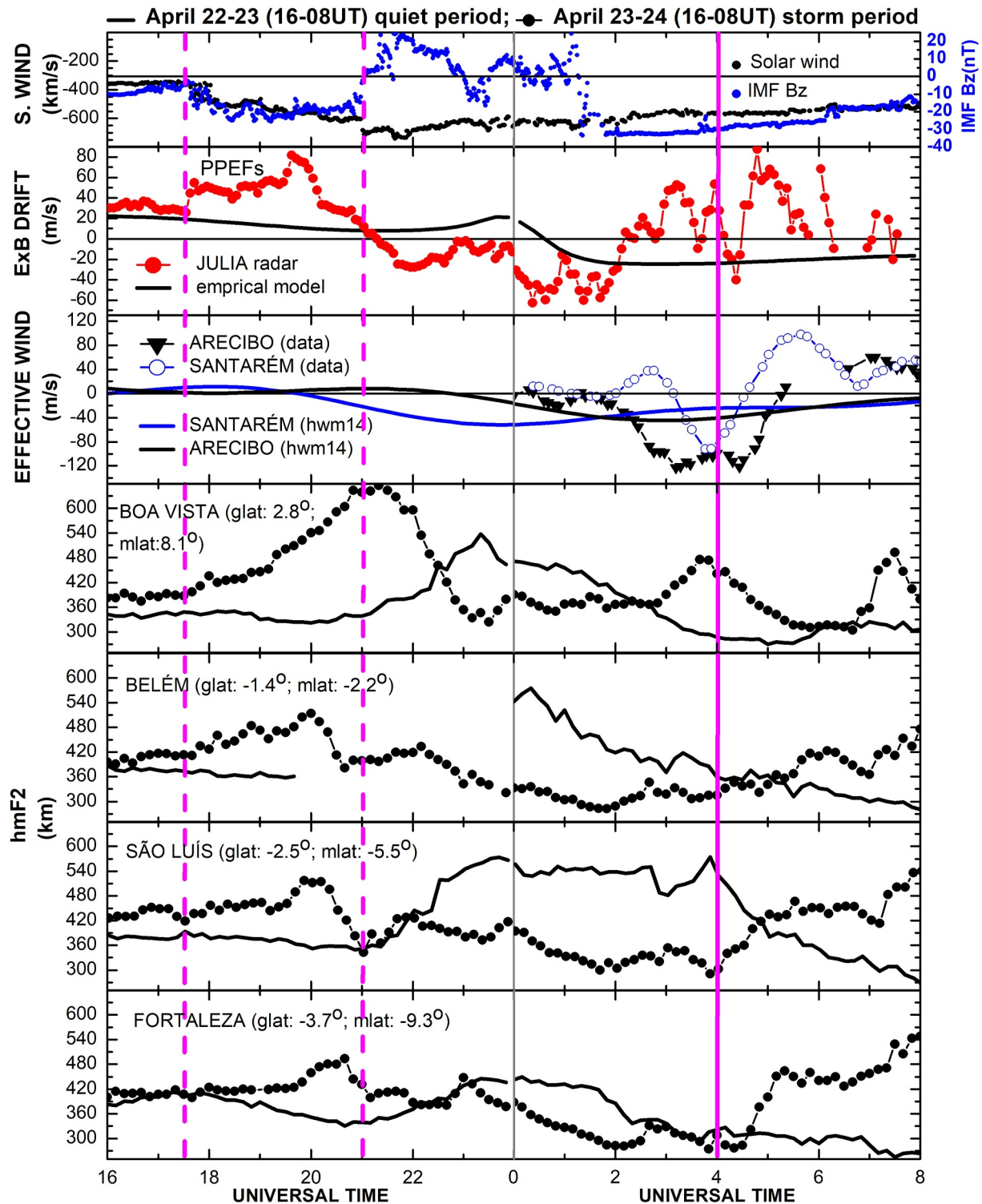
Figure 3. Group 1: Diurnal variations of geomagnetic activity indices solar wind speed and interplanetary magnetic field (B_z component) (first row); vertical $\mathbf{E} \times \mathbf{B}$ drifts (second row); thermospheric neutral wind speeds at Arecibo and Santarém (third row). The following four rows show hmF2 values for Boa Vista, Belém, São Luís, and Fortaleza, respectively. Data are for 23 April (left panels) and 24 2023 (right panels).
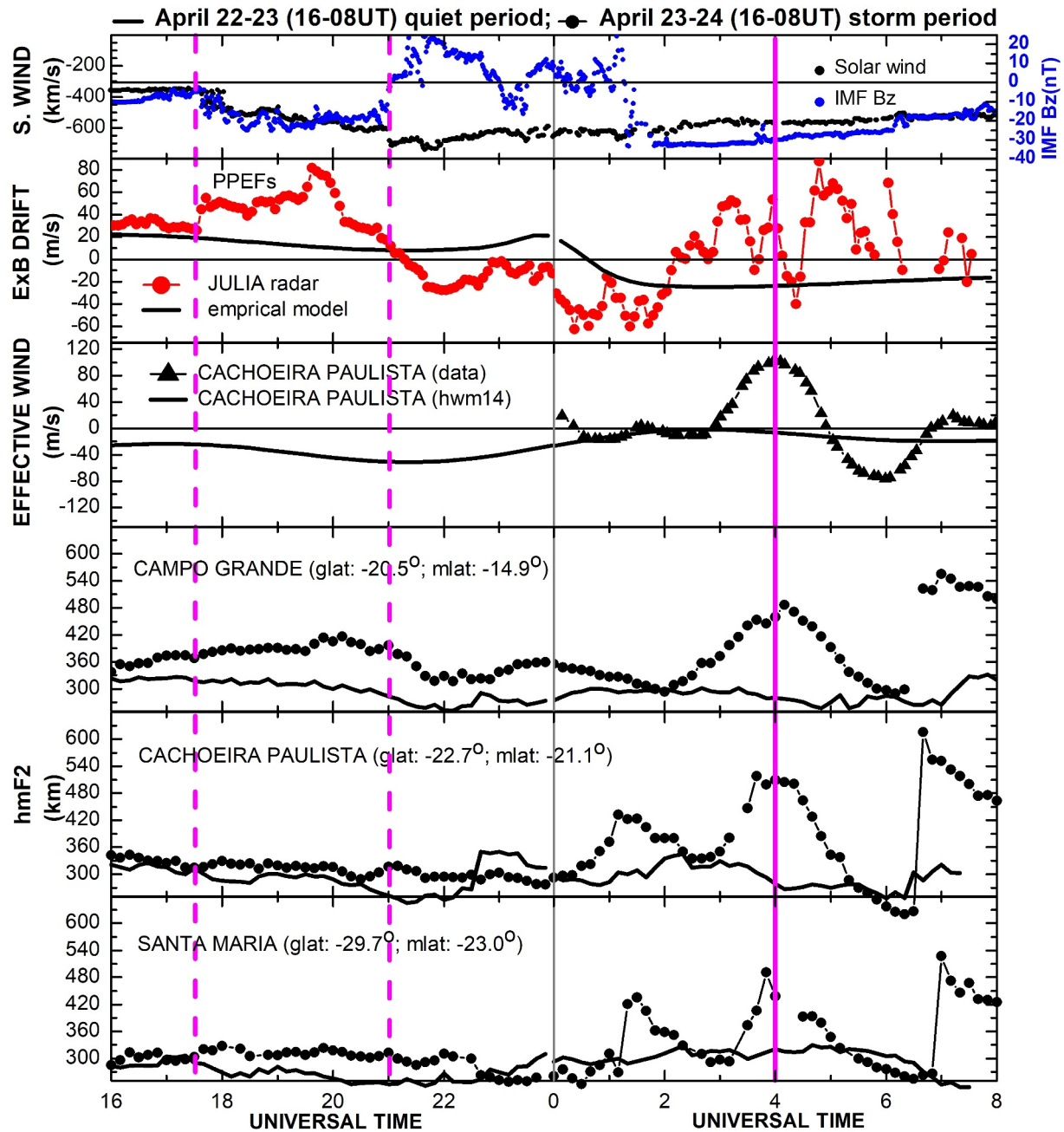
Figure 4. Group 2: the first two rows of panels are the same as Figure 3. The panels in row 3 are the thermospheric neutral wind speeds for Cachoeira Paulista (CP) and the next three rows show hmF2 values for Campo Grande, CP, and Santa Maria, respectively. Data are from 23 April (left panels) and 24 2023 (right panels).

descriptions and discussions of the ionospheric variations on 24 April (right panels) are presented at the end of this section. Considering the indicative indices of geomagnetic disturbance times (solar wind speed and IMF B_z) and $\mathbf{E} \times \mathbf{B}$ plasma drift as reference for our data analysis, they were repeated as in Figure 2. The continuous solid curves represent data or empirical results for 22–23 April, which is a period of geomagnetic quiet condition with absolute solar wind speed <400 km/s and IMF B_z < 5 nT. The first rapid increase of B_z to the south occurred at 17:30 UT on 23 April. Consequently, the $\mathbf{E} \times \mathbf{B}$ drift responds with an abrupt increment of 18 m/s compared to previous values, as well as compared to the drift values for calm conditions. This increase lasts 2 hr, reaching a maximum of 81 m/s at 19:37 UT. A detailed description of this storm electric field morphology was recently published by Fejer et al. (2024). All Group 1 hmF2 values increase following the $\mathbf{E} \times \mathbf{B}$ drift variations, including
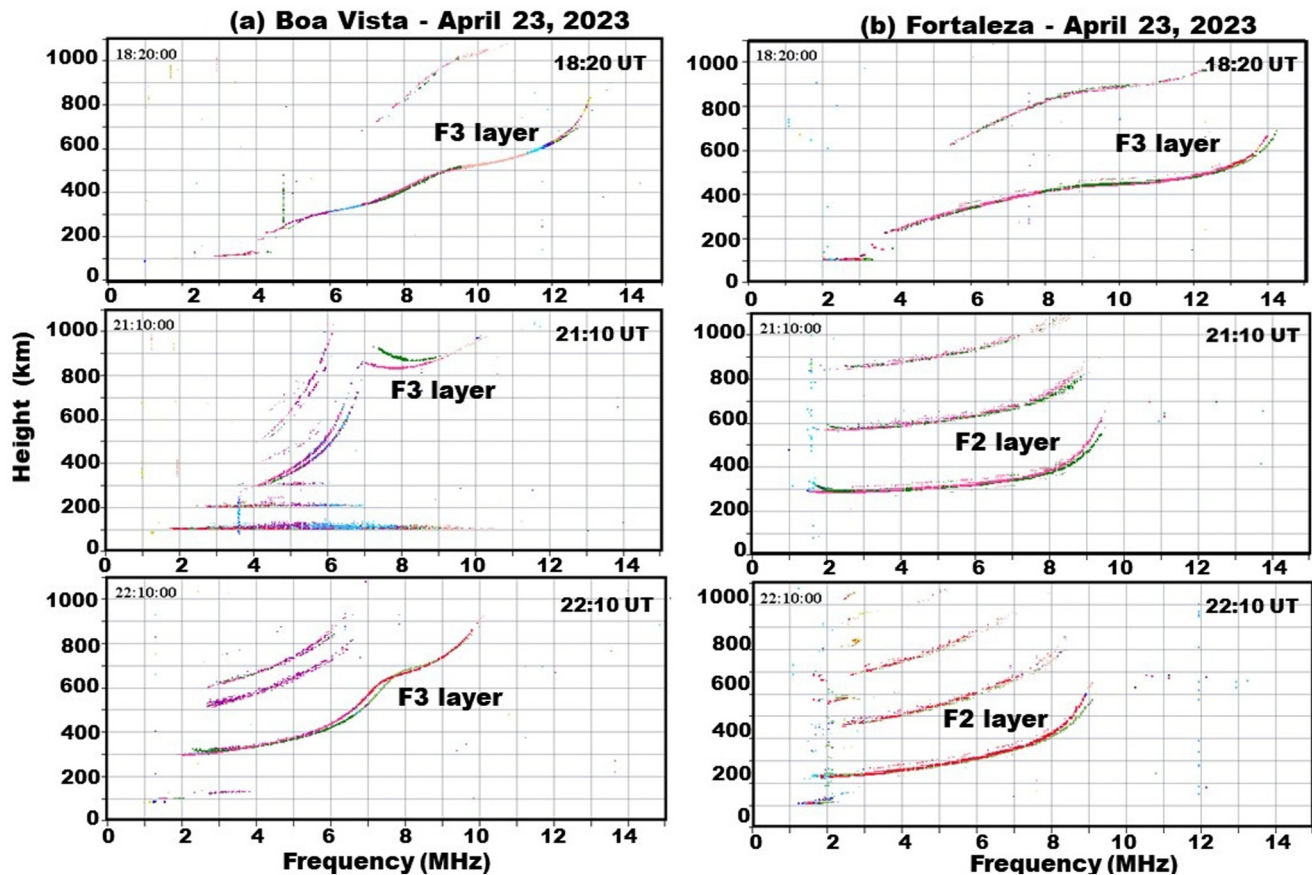
Figure 5. Ionograms over Boa Vista (a) and Fortaleza (b) during undershielding event on 23 April 2023 for 18:20, 21:10, and 22:10 UT.

the peak at 19:37 UT, which was better observed for locations with low magnetic inclination (BL and SL), as expected. However, the absence of abrupt increases in hmF2 may have been inhibited by competitive processes involving photoionization and ionic drag during the onset of PPEF (~14:30 LT). Such simultaneous elevation of the F layers is caused exclusively by an undershielding eastward electric field.

Balan et al. (2011, 2013) pointed out that TADs from the auroral oval can reach equatorial and low latitudes in 1.5 hr and their maximum effects occur around $\pm 16°$ magnetic latitude. Although wind waves or TADs do not have propagation preference during the day due to dissipation by ionic drag (Fuller-Rowell et al., 1994), hmF2 for BV, FZ (Figure 3), CG, CP, and SM (Figure 4—Group 2) present a response as if they were under the effects of such disturbed meridional winds. This can be observed by the maximum values around 3.5 hr after the start of the PPEF which are not correlated with the maximum in the $\mathbf{E} \times \mathbf{B}$ drift. The largest anticorrelation is clearly seen between the $\mathbf{E} \times \mathbf{B}$ drift and hmF2 for BV. It is observed that hmF2 increases at a similar rate even after the maximum $\mathbf{E} \times \mathbf{B}$ drift at 19:37 UT and during the beginning of overshielding event. An interesting point is that at FZ, even though it is not the BV conjugate point (only at the magnetic latitude almost opposite to BV), the large variations in hmF2 are not present.

One explanation is attributed to the asymmetry in thermospheric winds. Unfortunately, there are no wind measurements during the PPEF times, but it is possible to give an explanation based on the physical process of formation of the F3 layer (Balan & Bailey, 1995; Balan et al., 1997, 1998; Batista et al., 2017). Both BV and FZ are in the latitudinal range favorable to the formation of the F3 layer (Balan & Bailey, 1995). Furthermore, an appropriate combination of eastward electric field and equatorward winds is also required for the F3-layer formation. Batista et al. (2017) pointed out the development of the F3 layer in conjugate locations during geomagnetically disturbed times. Figures 5a and 5b show ionograms recorded during such an undershielding event with presence of F3 layer for BV (left panels) and FZ (right panels), respectively. The ionograms are for 18:20, 21:10, and 22:10 UT.

BV and FZ are not on the same magnetic meridian, however, it is reasonable to consider that the PPEF is constant in this longitudinal range. Thus, the well-defined F3 layer for the BV sector and, consequently, the high values of hmF2 are due to the disturbance of the thermospheric wind and with higher speeds over BV than over FZ. hmF2 values over BV remain high even after electric field reversal due to overshielding at 21:10 UT, while the F3 layer over FZ disappears and hmF2 decreases during the time (seen in Figure 3). This is the consequence of the obvious wind reversal toward the south, around FZ.

Figures 6 and 7 are similar to Figures 3 and 4, except that foF2 and TEC are shown instead of hmF2. The TEC axes are on the right side and the corresponding values are in blue. In general, all oscillations in foF2 are also seen in TEC, as expected. The relationship between perturbed foF2 compared to the quiet time values versus perturbed TEC compared to its quiet time values is also the same for each location, that is, when one of these perturbed parameters is greater than its quiet time values, the same happens with the other. However, there is one exception. Such a relationship is not seen in BV during the strong F3 layer occurrences between 17:00 and 22:00 UT. In fact, the F3 layer mechanism spreads/distributes the plasma in the magnetic latitude versus altitude cross section (Balan & Bailey, 1995) accumulating it on the top side of the F region. Thus, while observed critical frequencies decrease, vertical plasma integrations (TEC) increase.

The overshielding event begins at 21:10 UT and during this time causes downward vertical drift. The vertical drift shows rapid decreases after 21:10 UT following a different trend than the quiet time variations, as can be seen in Figure 2 or in Figures 3, 6, and 7. Its maximum descending value is -27 m/s at 22:00 UT. This converges with expected variations due to an overshielding action. It can be said that the DD can also produce the same drift, that is, an $\mathbf{E} \times \mathbf{B}$ plasma drift due to an electric field to the west (a downward drift at Earth's dayside). Considering that the B_z component had a turn to the north, then the energy input in the polar cap sector decreased, consequently, the contribution of DD should have caused a low or a decreasing effect also on the downward drift. That is, the drift should tend toward the quiet time values. Therefore, the absence of a coherent portion of DD, as recorded by the JULIA radar, implies the dominance of the overshielding electric field.

Ionospheric effects due to overshielding are also seen in other parameters over the locations with low magnetic inclination (I) that are in Group 1. The hmF2 values over BL, SL, and FZ begin to decrease before the B_z inversion at 21:10 UT (see Figure 3). This means that the F layer plasma moves downwards when the undershielding is weakening (decreasing vertical drift) to where the recombination rate increases (Balan et al., 2013). Consequently the critical frequency of the F region (foF2) also decreases (see Figure 6). The same dynamics of the F region are observed in BV, but with a two-hour delay due to the F3 layer formation process, as mentioned above.

The ionospheric peak parameters for Group 2 locations present different variations than Group 1. The hmF2 values do not change significantly and both foF2 and TEC begin to decrease just 1 hour after the B_z inversion at 21:10 UT (see Figures 4 and 7). This reveals that the strong northward meridional neutral wind may be compensating for the low downward $\mathbf{E} \times \mathbf{B}$ drift force, preventing the plasma from reaching lower altitudes with high levels of recombination. Group 2 sites have high magnetic inclination and this is the reason for the low $\mathbf{E} \times \mathbf{B}$ vertical drift force at these locations.

The $\mathbf{E} \times \mathbf{B}$ plasma drift, TEC and ionospheric peak parameters from late 23 April to 2 UT of 24 April exhibit typical variations of a storm day with the presence of a DD that causes inhibition of pre-reversal enhancement (Abdu et al., 2006). Therefore, no elevation of the F layer was observed as can be seen in Figures 3 and 4. The hmF2 values decrease (increase) during the disturbed (quiet) condition for all locations in Groups 1 and 2 with low magnetic inclination. Figures 6 and 7 show coherent responses of foF2 and TEC to the overshielding electric field with decreasing variations, except for some superimposed oscillation.

Thermospheric neutral wind speeds were observed simultaneously over AR, ST, and CP before sunrise on 24 April (third rows in Figures 6 and 7; see also Figure 1). Maximum transient equatorward winds of 100 m/s at 4 UT were recorded at AR and ST. The physical explanation for the origin of the wind disturbance with maximum value in AR in phase with maximum in ST is not simple. Apparently, this observation is sufficient to reject a TAD event as causal for the winds at each sight since such an event should pass through AR and subsequently through ST. These two locations are 2820 km apart, considering an observation altitude of 250 km.

Even so, the TAD passages were only confirmed by the analysis of the keogram in the TEC, which discovered for the first time, the interactions of the TADs when they reach equatorial and low latitudes (see details in the next section). It was observed that the $\mathbf{E} \times \mathbf{B}$ plasma drift changed from negative (down) to positive (up) values during
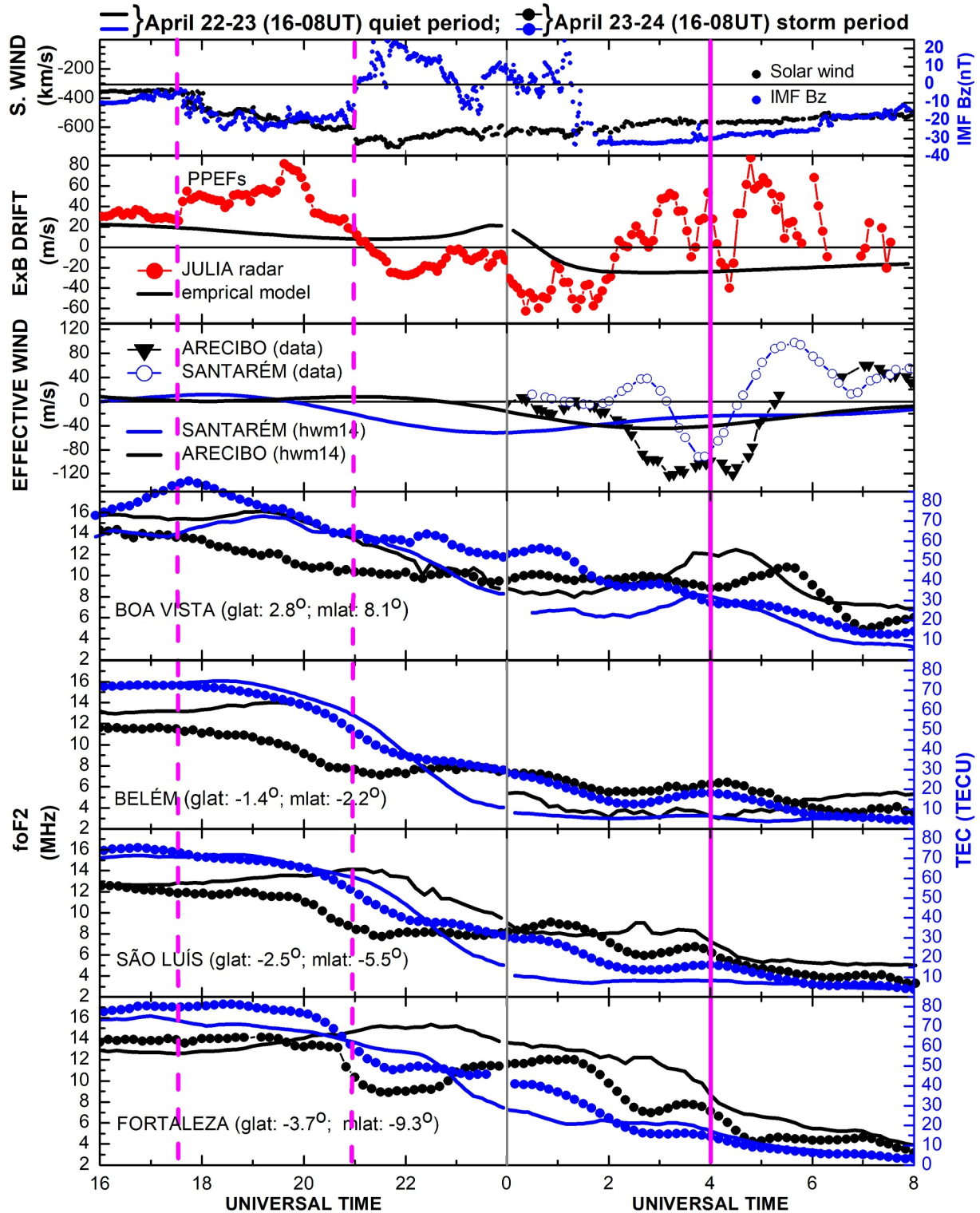
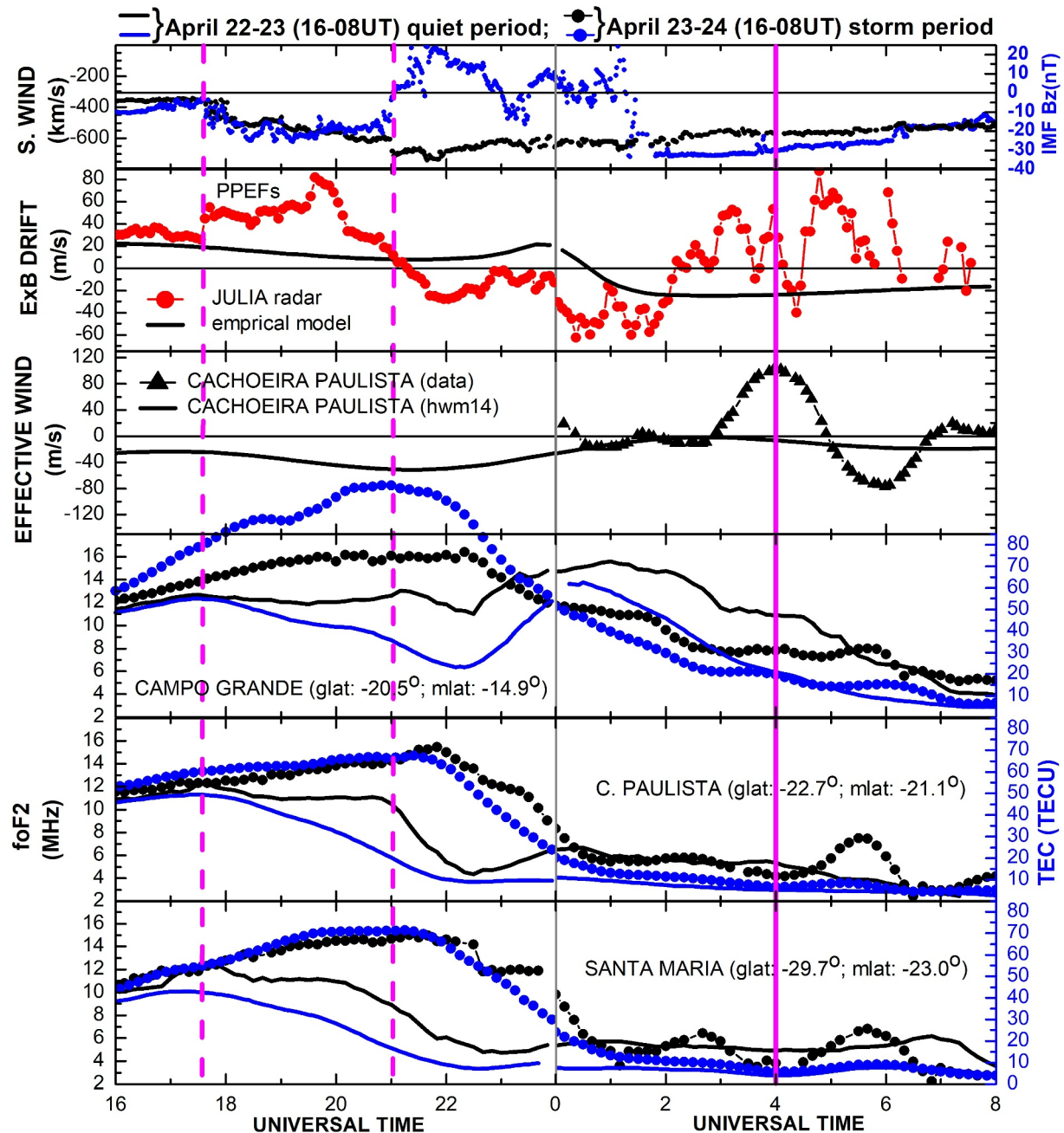**Figure 6.** The same as Figure 3, but for foF2 and TEC.

Figure 7. The same as Figure 4, but for foF2 and TEC.

the TAD events, but the ionospheric parameters do not respond to such variations. This is evidence of the dominance of the wind in the Brazilian sector.

Fejer et al. (2024) also discussed the same storm and pointed out plasma irregularities in the JULIA radar measurements due to these $\mathbf{E} \times \mathbf{B}$ plasma drift variations. The ionograms from all Brazilian Digisondes did not record spread F. Once again, the data confirm longitudinal differences in the American ionosphere during this large geomagnetic storm. The reactions of hmF2, foF2, and TEC to the TAD event are clearly seen at stations in Groups 1 and 2 where the magnetic inclination is large enough for the neutral wind to move the ionosphere layers up or down.

Maximum wind speeds toward the Equator produced well-defined maxima (minima) in hmF2 (foF2 and TEC) at 4 UT on 24 April. The foF2 and TEC minima are due to local plasma transport, driven by the motion of the meridional winds. The winds reverse direction after 4:30 UT, so the behavior of the mentioned ionospheric parameters also reverses. It is important to note that as soon as the conversion of the wind direction toward the poles occurs, the plasma moves downwards along the magnetic field lines and before being destroyed by recombination, it accumulates. Therefore, maxima appear in foF2 and TEC, as shown in Figures 6 and 7. The ionospheric effects due to disturbed thermospheric wind over South America were discussed by Batista et al. (2012) and Bravo et al. (2019). A maxima in the ionospheric densities were explained by traveling waveform winds.

Small minima in hmF2 were observed over SL and FZ close to 4 UT, when wind speeds are maximum, and the foF2-TEC duo also presented maximum values. These two locations already have significant I values (MLat = −5.5° and MLat = −9.3°, respectively) for the winds to cause their effects. Based on wind measurements in AR and ST, as well as variations in the mentioned parameters, it is concluded that the northerly winds crossed AR, ST, and remained in a southerly direction over BL, SL, and FZ. Considering the wind speed observed over CP and all ionospheric measurements in SM, CP, and CG confirm the presence of wind to the north places, this seems that a wind convergence occurred between FZ (MLat = −9.3°) and CG (MLat = −14.9°). Furthermore, unexpected wave interactions were observed between these locations. See details about this later in the keogram analysis.

3.2. Ionospheric Effects Due To Storm Electric Fields and TAD Event by Keogram Analysis

Figures 8a and 8b show the keogram for the meridian 67°W. Panels left-right of Figure 8a show ΔTEC for the evening-morning of 22–23 April and Figure 8b is the same as Figure 8a but for 23–24 April. ΔTEC showed only fluctuations in time (−6 to +6 TECU) on 22–23 April mainly after midnight for the equatorial and low-latitude sectors. In contrast, latitudinal propagation structures were clearly observed on selected days of the storm. First, poleward double structures are seen between 20:00 and 21:30 UT to the north and south, respectively. Such ionospheric plasma dynamics represents the expansions of the Equatorial Ionization Anomaly (EIA) crests as marked by pink arrows and shown in Figure 8b, left side panel. The keogram in the right panel of Figure 8b shows the effects of propagating wave structures from higher to lower latitudes. Structures are identified by pink arrows 1–3 and 4–6 for the northern and southern hemispheres, respectively. Transequatorial and northward structures were seen after 4 UT and are identified by pink dashed arrows 7–8. A better description of these waves is provided at the end of this section.

It is important to mention that positive ΔTEC occurs when weak smoothed TEC ($\overline{\text{TEC}}_{1h00}$) is smaller than strong smoothed TEC ($\overline{\text{TEC}}_{3h20}$) while negative means the opposite. Thus, the positive values marked by the pink arrows showing the EIA expansion, as mentioned above, indicate that decreasing TEC structures are moving from the magnetic equator to higher latitudes. The disturbed electric field to the east produces a disturbed fountain effect, and consequently the expansion of the EIA.

Figure 9 also shows the ΔTEC keograms, but for the 54°W meridian. Unfortunately, there are no data for latitudes higher than 10°N and 36°S. The propagation structures observed at the 67°W meridian and due to the PPEF (on 23 April) are not seen along 54°W meridian. However, that does not mean that there is no expansion of the EIA on the 54°W meridian. If the TEC changes slowly over time, our keogram technique will not accurately identify any structure.

The TEC results presented in Figure 10 confirm that the EIA expands rapidly at the 67°W meridian (left panel) and slows down at the 54°W meridian (right panel). The differences can be explained by longitudinal variations in effective wind speed and $\mathbf{E} \times \mathbf{B}$ background plasma drift that produce longitudinal variations in plasma density in this sector (De Paula et al., 2002; Nogueira et al., 2013).

Kelley et al. (2004) discussed the ionospheric effects due to a strong PPEFs, which causes superfountain effects (Balan et al., 2009) where the EIA crest can expand poleward. In our studied event, for the meridian located at 67°W, the north and south crests move from near the magnetic equator to latitudes of 18° and 20°, respectively.

Ionospheric effects due to an overshielding electric field are noticed at 22:00 UT, when ΔTEC rapidly changes to negative values covering a large latitudinal distribution, but with exceptions (see left panels of Figures 8b and 9).
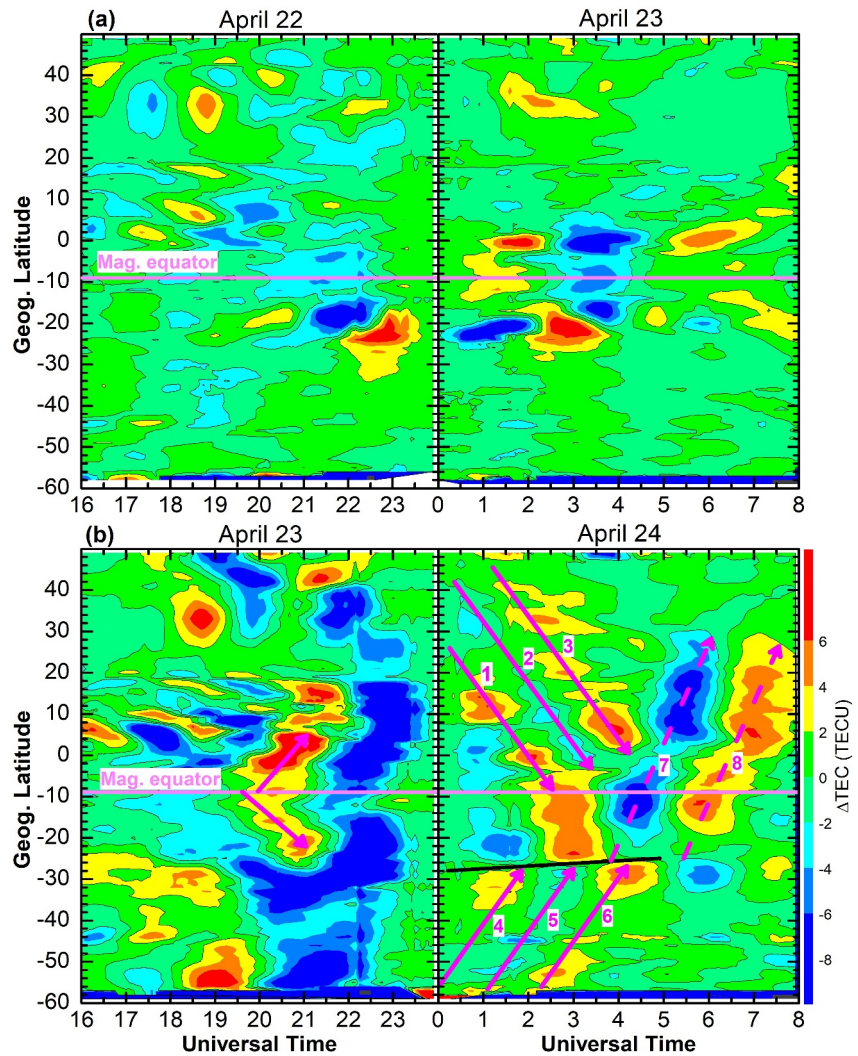
Figure 8. (a) Meridional keogram of ΔTEC for 67°W meridian and evening-morning of 22–23 April; (b) the same as (a) but for 23–24 April.

The variations are not rapid around the magnetic equator and also in the BV (2.8°N) sector, as seen more clearly in Figure 9, which shows the keogram for the 54°W meridian. The physical reasons for this ΔTEC behavior begin with the fountain effect, which due to the undershielding event, spreads the plasma in the cross section latitude versus altitude (Balan et al., 2018). After the electric field reverses, the plasma returns downwards and accumulates over a short period before being destroyed by recombination. The highest spread levels occur near the equatorial sector and where a strong F3 layer is developed.

The wave structures observed in the meridional keograms for ΔTEC (Figures 8b and 9, right side) are caused by TADs. Using visual examination, the northern propagation of the TAD is marked by the 1–2–3 arrows that correspond to the crest-trough-crest of the wave. This procedure was also used by Pradipta et al. (2016). The arrows are equidistant and have the same inclination, so the propagation speed ($V_\varnothing^N$), period (τ^N) and wavelength (λ^N) were determined by the arrow's slopes, time variation between the crests and $\lambda^N = \tau^N V_\varnothing^N$, respectively. The values are: $V_\varnothing^N = 470$ m/s; $\tau^N = 2.42$ hr and $\lambda^N = 4,095$ km. The same criteria were applied to obtain wave parameters for the southern hemisphere (arrows 4–5–6) and for the resulting wave after interaction (arrows 7–8). The respective values, with "S" superscript and "AI," are: $V_\varnothing^S = 485$ m/s; $\tau^S = 2.30$ hr and $\lambda^S = 4,016$ km; $V_\varnothing^{AI} = 763$ m/s; $\tau^{AI} = 3.22$ hr and $\lambda^{AI} = 8,845$ km. The last period was calculated by doubling the time variation
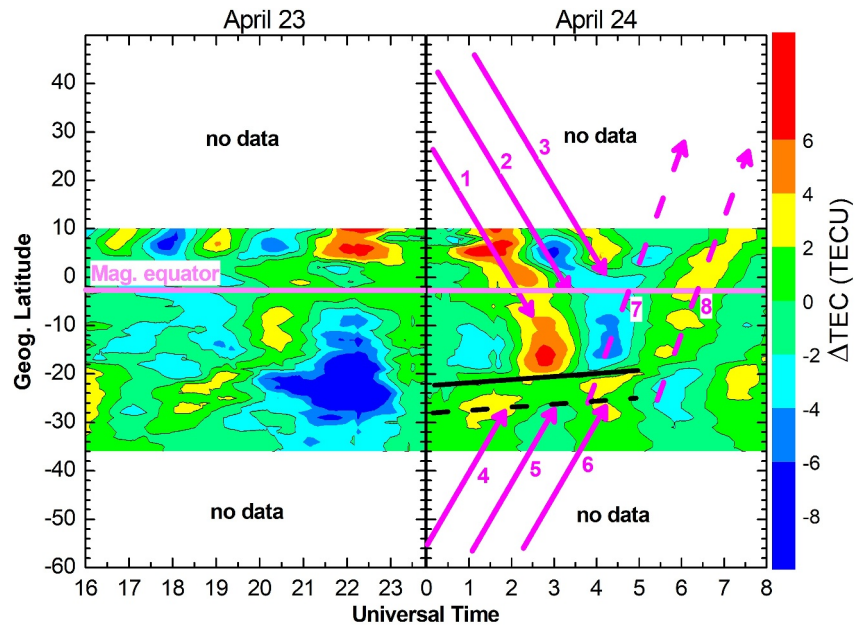
Figure 9. The same as Figure 8b, but for 54°W meridian.

between the trough and the crest. All of these values are in agreement with published results (Figueiredo et al., 2017; Gardner & Schunk, 2010; Hocke & Schlegel, 1996; Hunsucker, 1982).

Explanations are given here for two important questions: (a) Why do maximum wind speeds at such distant locations, such as AR and ST, occur at the same time (at 4 UT—see Figure 3)? And (b) Why do hmF2 maxima at separate locations in the Southern Hemisphere, such as CG, CP, and SM, also occur simultaneously (at 4 UT—see Figure 4)? Both responses are given by wave interactions as revealed in the meridional keogram for ΔTEC (Figures 8b and 9 right sides). The interactions or wave shock begin around 1 UT and near the latitude of −29°, as marked by the black line. First, it appears that the northern and southern propagations cancel each other out at 1
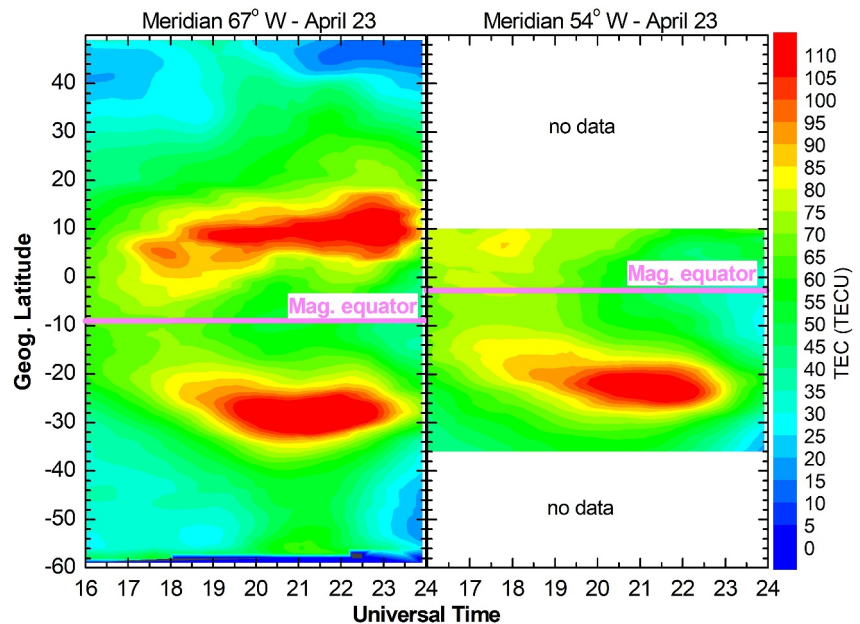

Figure 10. Latitudinal distribution of total electron content with the time for the meridians 67°W (left side) and 54°W (right) during 23 April.

UT. Just 1 hour later, the interactive process reaches the magnetic equator and, consequently, propagation decreases over time and the amplitude of the wave between the magnetic equator and where the shock is occurring is intensified. The crest of the northern wave is blocked above the magnetic equator between 3 and 4 UT and an apparent northward reflection begins around 4 UT at latitude = −26°. The new reflected wave has a greater propagation speed, period and wavelength than the original, as quantified above. Therefore, the coincident maxima in wind speeds in AR and ST are explained by interactive processes that modify the original north wave near ST by altering the propagation speed or disrupting it and causing reflection. A similar answer can be given to justify the simultaneity in hmF2 peaks in the southern CG, CP and SM regions, however, the consequence of the interactive process that leaves the wave in phase over a large latitudinal band in the southern hemisphere, as deduced from keograma, is the main cause.

The right panel of Figure 9 shows the keogram for the 54°W meridian, which crosses closer to our measurement locations than the 67°W meridian. The positions of the arrows are, for comparison purposes, the same as in Figure 8b. In general, the wave characteristics remain the same as at the 67°W meridian, but the locations and times of the events are different, for example, the shock line rose 6° (displacement is represented by black, dashed and solid lines). The last results are much more in line with what is expected from the Digisonde and TEC measurements due to the wind speeds.

Considering around 4 UT as our reference time and comparing the measurements presented in Figure 9 (right side) with those in Figures 3, 4, 6, and 7, we notice coherently positive (negative) ΔTEC values, which correspond to an increase (decrease) in hmF2 and a decrease (increase) in foF2-TEC, over BV, CG, CP, and SM (SL and FZ). In addition, it is also fascinating to consider what happened along the shock line and below. Wave shocks begin at −22°, near 1 UT and advance over time to −19° at 5 UT. The measurements for CG (GLat = −20.5°) happily cross this line. As the CG is located above the shock line at 1 UT, the ionospheric effects are not due to the original southerly winds, however, the location is reversed to below the shock line before 4 UT. This explains why the Digisonde parameters are not in phase when comparing CG data with CP and SM. The ionosphere in the latter two places was purely controlled by the original southerly winds or equatorward winds.

Furthermore, two more coherent associations must be highlighted: the explanation why the shock line has a displacement of 6° for the keogram of 54°W, compared to 67°W, is related to the different displacements between the geographic coordinates and magnetic in the corresponding meridians which is also 6°, as calculated by IGRF13. Considering that the positions of the TAD sources that are in the boreal and southern auroral oval have the same positions displaced from the geographic coordinates, the convergent positions of the waves (shock line) are justified; the slope of the shock line is 22 m/s and can be attributed to differences between the southern and northern propagation velocities. Obviously, positive values mean greater southern propagation than northern propagation. For example, the fast wave advances further in latitude/space over time to reach the cancellation point than the slow wave. This is consistent with the values calculated here ($V_\varnothing^N - V_\varnothing^S$) which is 15 m/s.

We are not certain why the shock line is 20° below the magnetic equator. It may be due to the eccentricity of the Earth's magnetic axis relative to the rotational axis, hence asymmetric positions of the northern and southern auroral ovals and/or an asymmetry in the expansions of the northern and southern auroral ovals during this storm.

4. Conclusions

A keogram using a strong average (3h20 min bin) on TEC was able to amplify the large-scale ionospheric signatures of PPEFs and TADs during the 23–24 April 2023 geomagnetic storm.

In addition to the well-known ionospheric variations due to under- and overshielding events, the role of the F3 layer mechanism during the geomagnetic disturbance was identified. The F3 layer process spreads the plasma, mainly in altitude, accumulating it in the topside of the F region. Thus, although the observed critical frequencies decrease, the plasma vertical integrations (TEC) increase.

The ionospheric response to both storm electric fields and TADs showed clear longitudinal dependence. The expansion of the EIA is faster on the 67°W meridian than on the 54°W meridian. The positions of the wave shock lines, seen in the keograms for each meridian mentioned, followed the respective displacements between the geographic and magnetic equators; consequently, the resulting interferences are also displaced in the localities. A convincing point about this is that the variations observed in thermosphere (wind speed) and ionospheric

parameters (foF2, hmF2, and TEC) recorded by instruments spread across different locations in Brazil are only consistent with the keogram of the 54°W meridian that crosses the most centralized sector in the country.

Our conclusions are supported by known phenomenologies and mainly by multi-instrument measurement redundancies. However, modeling studies are necessary to fully understand TAD interference and its consequences.

Data Availability Statement

Equatorial vertical plasma drift from JULIA radar can be find online in Madrigal database at (http://cedar.openmadrigal.org/) by MIT Haystack Observatory. The Digisonde data can be downloaded from the University of Massachusetts Lowell DIDB database of Global Ionospheric Radio Observatory (https://giro.uml.edu/didbase/scaled.php) whose PI is Inez S. Batista from INPE. All raw Fabry-Perot interferometer data used in this research are available without restriction through Kerr et al. (2023). The IMF B_z from SuperMAG at https://supermag.jhuapl.edu/indices/ and Kp index produced by Geomagnetic Observatory Niemegk, GFZ German Research Centre for Geosciences are available at https://www.gfz-potsdam.de/en/section/geomagnetism/topics/geomagnetic-observatories. GNSS data from the networks CORS/USA, RBMC/Brazil, INCT/Brazil, and RAMSAC/Argentina are also online at https://geodesy.noaa.gov/, https://www.ibge.gov.br/geociencias/informacoes-sobre-posicionamento-geodesico/rede-geodesica, http://is-cigala-calibra.fct.unesp.br/, https://www.ign.gob.ar/NuestrasActividades/Geodesia/Ramsac/DescargaRinex, respectively.

References

Abdu, M. A., de Souza, J. R., Sobral, J. H. A., & Batista, I. S. (2006). Magnetic storm associated disturbance dynamo effects in the low and equatorial latitude ionosphere. In B. Tsurutani, R. McPherron, G. Lu, J. H. A. Sobral, & N. Gopalswamy (Eds.), *Recurrent magnetic storms: Corotating solar wind streams*. https://doi.org/10.1029/167GM22

Alken, P., Thébault, E., Beggan, C. D., Amit, H., Aubert, J., Baerenzung, J., et al. (2021). International geomagnetic reference field: The thirteenth generation. *Earth Planets and Space*, *73*(1), 49. https://doi.org/10.1186/s40623-020-01288-x

Balan, N., & Bailey, G. J. (1995). Equatorial plasma fountain and its effects: Possibility of an additional layer. *Journal of Geophysical Research*, *100*(A11), 21421–21432. https://doi.org/10.1029/95JA01555

Balan, N., Bailey, G. J., Abdu, M. A., Oyama, K. I., Richards, P. G., MacDougall, J., & Batista, I. S. (1997). Equatorial plasma fountain and its effects over three locations: Evidence for an additional layer, the F₃ layer. *Journal of Geophysical Research*, *102*(A2), 2047–2056. https://doi.org/10.1029/95JA02639

Balan, N., Batista, I. S., Abdu, M. A., MacDougall, J., & Bailey, G. J. (1998). Physical mechanism and statistics of occurrence of an additional layer in the equatorial ionosphere. *Journal of Geophysical Research*, *103*(A12), 29169–29182. https://doi.org/10.1029/98JA02823

Balan, N., Otsuka, Y., Nishioka, M., Liu, J. Y., & Bailey, G. J. (2013). Physical mechanisms of the ionospheric storms at equatorial and higher latitudes during the recovery phase of geomagnetic storms. *Journal of Geophysical Research: Space Physics*, *118*(5), 2660–2669. https://doi.org/10.1002/jgra.50275

Balan, N., Shiokawa, K., Otsuka, Y., Watanabe, S., & Bailey, G. J. (2009). Super plasma fountain and equatorial ionization anomaly during penetration electric field. *Journal of Geophysical Research*, *114*(A3), A03310. https://doi.org/10.1029/2008JA013768

Balan, N., Souza, J., & Bailey, G. J. (2018). Recent developments in the understanding of equatorial ionization anomaly: A review. *Journal of Atmospheric and Terrestrial Physics*, *171*, 3–11. https://doi.org/10.1016/j.jastp.2017.06.020

Balan, N., Yamamoto, M., Liu, J. Y., Otsuka, Y., Liu, H., & Lühr, H. (2011). New aspects of thermospheric and ionospheric storms revealed by CHAMP. *Journal of Geophysical Research*, *116*(A7), A07305. https://doi.org/10.1029/2010JA016399

Batista, I. S., Abdu, M. A., Nogueira, P. A. B., Paes, R. R., de Souza, J. R., Reinisch, B. W., & Rios, V. H. (2012). Early morning enhancement in ionospheric electron density during intense magnetic storms. *Advances in Space Research*, *49*(11), 1544–1552. https://doi.org/10.1016/j.asr.2012.01.006

Batista, I. S., Candido, C. M. N., Souza, J. R., Abdu, M. A., de Araujo, R. C., Resende, L. C. A., & Santos, A. M. (2017). F₃ layer development during quiet and disturbed periods as observed at conjugate locations in Brazil: The role of the meridional wind. *Journal of Geophysical Research: Space Physics*, *122*(2), 2361–2373. https://doi.org/10.1002/2016JA023724

Bravo, M. A., Batista, I. S., Souza, J. R., & Foppiano, A. J. (2019). Ionospheric response to disturbed winds during the 29 October 2003 geomagnetic storm in the Brazilian sector. *Journal of Geophysical Research: Space Physics*, *124*(11), 9405–9419. https://doi.org/10.1029/2019JA027187

de Paula, E. R., Souza, J. R., Fejer, B. G., Bailey, G. J., & Heelis, R. A. (2002). Longitudinal ionospheric effects in the South Atlantic evening sector during solar maximum. *Journal of Geophysical Research*, *107*(A7), 1119. https://doi.org/10.1029/2001JA000298

Drob, D. P., Emmert, J. T., Meriwether, J. W., Makela, J. J., Doornbos, E., Conde, M., et al. (2015). An update to the Horizontal Wind Model (HWM): The quiet time thermosphere. *Earth and Space Science*, *2*(7), 301–319. https://doi.org/10.1002/2014EA000089

England, S. L., Greer, K. R., Zhang, S.-R., Evans, S., Solomon, S. C., Eastes, R. W., et al. (2021). First comparison of traveling atmospheric disturbances observed in the middle thermosphere by Global-scale Observations of the Limb and Disk to traveling ionospheric disturbances seen in ground-based total electron content observations. *Journal of Geophysical Research: Space Physics*, *126*(6), e2021JA029248. https://doi.org/10.1029/2021JA029248

Fejer, B. G., Laranja, S. R., & Condor, P. (2024). Multi-process driven unusually large equatorial perturbation electric fields during the April 2023 geomagnetic storm. *Frontiers in Astronomy and Space Sciences*, *11*, 1351735. https://doi.org/10.3389/fspas.2024.1351735

Figueiredo, C. A. O. B., Wrasse, C. M., Takahashi, H., Otsuka, Y., Shiokawa, K., & Barros, D. (2017). Large-scale traveling ionospheric disturbances observed by GPS dTEC maps over North and South America on Saint Patrick's Day storm in 2015. *Journal of Geophysical Research: Space Physics*, *122*(4), 4755–4763. https://doi.org/10.1002/2016JA023417

Fuller-Rowell, T. J., Codrescu, M. V., Moffett, R. J., & Quegan, S. (1994). Response of the thermosphere and ionosphere to geomagnetic storms. *Journal of Geophysical Research*, *99*(A3), 3893–3914. https://doi.org/10.1029/93ja02015

Gardner, L. C., & Schunk, R. W. (2010). Generation of traveling atmospheric disturbances during pulsating geomagnetic storms. *Journal of Geophysical Research*, *115*(A8), A08314. https://doi.org/10.1029/2009JA015129

Guo, J., Liu, H., Feng, X., Wan, W., Deng, Y., & Liu, C. (2014). Constructive interference of large-scale gravity waves excited by interplanetary shock on 29 October 2003: CHAMP observation. *Journal of Geophysical Research: Space Physics*, *119*(8), 6846–6851. https://doi.org/10.1002/2014JA020255

Hocke, K., & Schlegel, K. (1996). A review of atmospheric gravity waves and travelling ionospheric disturbances: 1982–1995. *Annales Geophysicae*, *14*(9), 917–940. https://doi.org/10.1007/s00585-996-0917-6

Hunsucker, R. D. (1982). Atmospheric gravity waves generated in the high-latitude ionosphere: A review. *Reviews of Geophysics*, *20*(2), 293–315. https://doi.org/10.1029/RG020i002p00293

Hysell, D. L., & Burcham, J. D. (1998). JULIA radar studies of equatorial spread F. *Journal of Geophysical Research*, *103*(A12), 29155–29167. https://doi.org/10.1029/98JA02655

Kelley, M. C. (Ed.) (2009)., *The Earth's ionosphere: Plasma physics and electrodynamics* (2nd edn.). International Geophysics, Academic Press.

Kelley, M. C., Vlasov, M. N., Foster, J. C., & Coster, A. J. (2004). A quantitative explanation for the phenomenon known as storm-enhanced density. *Geophysical Research Letters*, *31*(19), L19809. https://doi.org/10.1029/2004GL020875

Kerr, R. B., Kapali, S., Harding, B. J., & Souza, J. R. (2023). Spectral contamination of the 6300Å emission in single-etalon Fabry-Perot interferometers Data. *Zenodo*. https://doi.org/10.5281/zenodo.8225839

Nogueira, P. A. B., Abdu, M. A., Souza, J. R., Bailey, G. J., Batista, I. S., Shume, E. B., & Denardini, C. M. (2013). Longitudinal variation in Global Navigation Satellite Systems TEC and topside ion density over South American sector associated with the four-peaked wave structures. *Journal of Geophysical Research: Space Physics*, *118*(12), 7940–7953. https://doi.org/10.1002/2013JA019266

Oliveira, C. B., Espejo, T. M. S., Moraes, A., Costa, E., Sousasantos, J., Lourenço, L. F. D., & Abdu, M. A. (2020). Analysis of plasma bubble signatures in total electron content maps of the low-latitude ionosphere: A simplified methodology. *Surveys in Geophysics*, *41*(4), 897–931. https://doi.org/10.1007/s10712-020-09584-7

Pradipta, R., Valladares, C. E., Carter, B. A., & Doherty, P. H. (2016). Interhemispheric propagation and interactions of auroral traveling ionospheric disturbances near the equator. *Journal of Geophysical Research: Space Physics*, *121*(3), 2462–2474. https://doi.org/10.1002/2015JA022043

Scherliess, L., & Fejer, B. G. (1999). Radar and satellite global equatorial F region vertical drift model. *Journal of Geophysical Research*, *104*(A4), 6829–6842. https://doi.org/10.1029/1999JA900025